Electronic Supplementary Information

for

Highly Accessible and Dense Surface Single Metal FeN_4 Active Sites for Promoting Oxygen Reduction

Guangbo Chen, Yun An, Shengwen Liu, Fanfei Sun, Haoyuan Qi, Haofei Wu, Yanghua He, Pan Liu, Run Shi, Jian Zhang, Agnieszka Kuc, Ute Kaiser, Tierui Zhang, Thomas Heine, Gang Wu*, and Xinliang Feng**

Table of contents:

Chemicals

2, 6-diaminopyridine (DAP), $Zn(NO_3)_3 \cdot 6H_2O$, $Fe(NO_3)_3 \cdot 9H_2O$, cyanamide, silica colloid solution (12 nm, Ludox HS40), Nafion perfluorinated resin solution (5 wt. % in mixture of lower aliphatic alcohols and water, contains 45% water) were obtained from Sigma-Aldrich. KOH was purchased from VWR chemicals. Pt/C (20%) was purchased from FuelCellStore. All the reagents were of analytical grade and used as received without further purification. Deionized water was used throughout the experimental processes.

Synthesis of NHPC support

NHPC support was synthesized by a zinc-template synthetic strategy as developed by our group. First, DAP/Zn/SiO_2 solid composites were prepared by drying 15.0 g silica colloid solution (*ca*. 12 nm, Ludox HS40, 40% in water) containing 2.18 g DAP, and 2.38 g $Zn(NO_3)_2 \cdot 6H_2O$. Second, the obtained solid composites were thermally treated at 900 °C for 2 hours under a flowing nitrogen atmosphere. Third, the pyrolyzed sample was etched in hydrofluoric acid solution (10 wt%) for removing the silica templates. After drying, the NHPC support was achieved.

Synthesis of *sur*-FeN_4-HPC

100 mg NHPC powder was dispersed into an isopropanol solution (50% *v/v*) containing 5.0 mg $Fe(NO_3)_3 \cdot 9H_2O$ and 10.0 mg cyanamide. After 1 h ultrasonication and 10 h magnetic stirring at room temperature, the Fe^{3+} and cyanamide adsorbed NHPC was collected by centrifugation and then dried at 60 °C. Then, thermal activation was performed at 900 °C for 2 hours in a nitrogen flow to yield the *sur*-FeN_4-HPC electrocatalyst. No further acid leaching treatment is required.

Synthesis of FeN_4-HPC

b-FeN_4-NHPC was prepared by a one-pot zinc-mediated template synthesis strategy as that for NHPC while using DAP/ZnFe/SiO_2 solid composites as corresponding precursors. First, DAP/ZnFe/SiO_2 were prepared by drying 15.0 g silica colloid solution (~12 nm, Ludox HS40, 40% in water) containing 2.18 g DAP, 2.38 g $Zn(NO_3)_2 \cdot 6H_2O$ and 0.40 g $Fe(NO_3)_3 \cdot 9H_2O$ (molar ratio of Zn/Fe = 8/1). Second, the obtained solid composites were thermally treated at 900 °C for 2 hours under nitrogen atmosphere. Third, the pyrolyzed sample was etched in hydrofluoric acid solution (10 wt%) for simultaneously removing the silica templates and unstable Fe-containing species. After second pyrolysis at 900 °C for 2 hours in nitrogen atmosphere, the FeN_4-HPC electrocatalyst was obtained.

Characterizations

Powder XRD patterns were collected over on a Bruker D8 Focus X-ray diffractometer equipped with a Cu Kα radiation source (λ = 1.5405 Å). Raman spectra were recorded with a Bruker RFS 100/S spectrometer at a wavelength of 532 nm. TEM was performed using a LIBRA 200 MC Cs STEM (Carl Zeiss) tool operating at an acceleration voltage of 200 kV. Aberration-corrected HAADF-STEM images and energy-dispersive X-ray spectroscopy (EDX) spectra were acquired on a JEM-ARM300F S/STEM (JEOL) operating at 300 kV. Aberration-corrected HRTEM imaging was conducted on the SALVE microscope operated under 80 kV. ICP-OES data were collected on Varian 710. To prepare the samples for ICP-OES, samples were first calcined at 600 ºC for 6 h. Then the solid residues were dissolved in aqua regia ($HNO_3 \cdot 3HCl$)

at 60 ºC. Finally, the solutions were diluted to the ppm range for the ICP-OES measurements. N_2 adsorption-desorption experiments were conducted at 77 K on a Quantachrome SI-MP Instrument. All samples were degassed at 150 °C prior to measurements. XPS experiments were carried out on an AXIS Ultra DLD (Kratos) system using Al Kα radiation. Fe K-edge EXAFS data were collected in Fluorescence mode at beamline 14W1 at Shanghai Synchrotron Radiation Facility (SSRF). The XAFS raw data were processed with background-subtraction, normalization and Fourier transformation by the standard procedures with Athena module of the IFEFFIT software packages.[1] EXAFS fitting was performed by the Artemis module, following the EXAFS equation below:

$$\chi(k) = \sum_j \frac{N_j S_0^2 F_j(k)}{kR_j^2} \exp\left[-2k^2\sigma_j^2\right] \exp\left[\frac{-2R_j}{\lambda(k)}\right] \sin\left[2kR_j + \Phi_j(k)\right] \quad (1)$$

where S_0^2 is the amplitude reduction factor, $F_j(k)$ is the effective curved-wave backscattering amplitude, N_j is the number of neighbors in the j_{th} atomic shell, R_j is the distance between the X-ray absorbing central atom and the atoms in the j_{th} atomic shell, λ is the mean free path in Å, $\phi_j(k)$ is the phase shift, σ_j^2 is the Debye-Waller parameter of the j_{th} atomic shell (variation of distances around the average R_j).

Electrochemical measurements

All catalysts were prepared by mixing 10 mg of the catalysts in 1.0 mL of solution containing 480 μL of ethanol, 480 μL of H_2O and 40 μL of 5% Nafion solution, followed by ultrasonication for 30 min to form homogeneous catalysts inks. The obtained catalysts inks were then dropped on the surface of pretreated RDE surface and air-dried before the electrocatalytic tests, leading to a loading of 0.6 and 0.1 mg cm^{-2} for the obtained Fe-N-C electrocatalysts and Pt/C, respectively. All the electrochemical measurements were carried out on a WaveDriver 20 (Pine Research Instrumentation) and CHI 660E Potentiostat systems equipped with a three-electrode cell. A glassy carbon electrode (GCE) coated with the catalyst inks was served as the working electrode, an Ag/AgCl and a Pt wire were used as reference and counter electrode, respectively. All the measurements were performed at ambient temperature in a 0.1 M $HClO_4$ acidic electrolyte solution. Potentials in this work were all referred to RHE through the Nernst equation according to E (*vs.* RHE) = E (*vs.* Ag/AgCl) + 0.197 + 0.05916 × pH.

The hydrogen peroxide yield (H_2O_2 %) and electron transfer number (n) during the ORR can be determined by a rotating ring-disk electrode (RRDE) technique and calculated *via* the following equations:

$$H_2O_2(\%) = 200 \times \frac{\frac{I_r}{N}}{I_d + \frac{I_r}{N}} \quad (2)$$

$$n = 4 \times \frac{I_d}{I_d + \frac{I_r}{N}} \quad (3)$$

where I_d is the disk current, I_r is the ring current, and N is the current collection efficiency of the Pt ring (N = 0.37).

The accelerated durability tests of the electrocatalysts were performed in the O_2-saturated 0.1 M $HClO_4$ electrolyte solution at room temperature by applying potential cycling between 1.0 and 0.6 V *vs*. RHE with a sweep rate of 50 mV s^{-1}.

The electrochemical double-layer capacitance (C_{dl}) of the carbon-based material was determined from double layer charging curves in non-faradic potential range of 1.00 - 1.10 V (*vs*. RHE). The electrochemically active surface area (*ECSA*) was further calculated based on:

$$ECSA\ (m^2\ g^{-1}) = \frac{C_{dl}}{C_{GDE} \times L_{cata}} \qquad (4)$$

where C_{GDL} is the double layer capacitance of GCE (0.02 mF cm^{-2})[2] and L_{cata} is the catalyst loading amount (6.0 g m^{-2}).

Quantification of the accessible active sites

The accessible site densities of FeN_4 sites in the b-FeN_4-NHPC and e-FeN_4-NHPC were determined according to the method described by Kucernak et al.[3] The method is based on the adsorption and reduction of nitrite (NO_2^-) on the central Fe atoms of FeN_4 sites. The experiments required three stages, 1) Experiments without nitrite measuring the ORR LSV curves and the nitrite reduction region CV background; 2) Experiments with nitrite measuring ORR LSV curves and the nitrite reduction region CV; 3) Further experiments without nitrate to study catalyst recovery for ORR.

The accessible site density (*SD*), intrinsic turnover frequency (*TOF*) and utilization ratio of FeN_4 (U_{FeN4}) were calculated using the following equations:[3, 4]

$$SD\ (\text{site}\ g^{-1}) = \frac{Q_{strip} \times N_A}{n_{strip} \times F \times m_{cat}} \qquad (5)$$

$$TOF\ (s^{-1}) = \frac{n_{strip} \Delta j_k (\text{mA cm}^{-2})}{Q_{strip} (C\ g{-}1) L_c (\text{mg cm}^{-2})} \qquad (6)$$

$$U_{FeN4} = \frac{SD\ (site\ g^{-1}) \times M_{Fe}\ (g\ mol^{-1})}{N_A \times Fe\ wt\%} \qquad (7)$$

where Q_{strip} is the excess coulometric charge associated with the stripping peak, F is the Faraday constant, n_{strip} is the number of electrons associated with the reduction of one nitrite per site (n_{strip} = 5), j_k is the kinetic current density,

$j_k = \frac{j_{lim} \times j}{j_{lim} - j}$, $\Delta j_k = j_{k(unposioned)} - j_{k(poisoned)}$. L_C is the catalyst loading during the reversible nitrite poisoning experiments (0.27 mg cm^{-2}).

PEMFC tests

The cathode catalyst inks were dispersed by sonicating the catalyst, 1-proponal, de-ionized water, and Nafion® suspension in a bath sonicator for at least three hours. The inks were coated on an SGL 29BC gas diffusion layer (GDL) using a manual doctor blade technique until the cathode catalyst loading reached ~ 4.0 mg cm^{-2}. A commercial Pt-catalyzed gas diffusion electrode (0.20 mg_{Pt} cm^{-2}) was used as the anode. The cathode and the anode were hot-pressed

onto a Nafion 212 membrane at 130 °C for 5 min. The cell area is 5 cm^2. The single cell was then evaluated in a fuel cell test station (100W, Scribner 850e, Scribner Associates, Inc.). The cells were conditioned at 80 °C with 200 mL min^{-1} of N_2 in the anode and cathode for two hours to hydrate the membrane and ionomer. Air/O_2 flowing at 500 mL min^{-1} and H_2 (purity 99.999%) flowing at 300 mL min^{-1} were used as the cathode and anode reactants, respectively. The partial pressure of reactant gases at both electrodes was 1.0 bar. Fuel cell polarization curves were recorded in a potential control mode, and 100% relative humidity (RH) and cell temperature of 80°C were maintained. Durability tests were employed standard accelerated stress test for Fe-N-C catalysts by cycling voltage from 0.60 to 0.95 V under H_2/air condition at 100 RH% and 80°C for 30000 cycles.

Computational methods and details

All the calculations were carried out using Amsterdam Modeling Suite (AMS) package.[5] Density functional theory (DFT) with Perdew-Burke-Ernzerhof (PBE) exchange-correlation functional[6] and the valence triple-zeta polarized (TZP) basis sets composed of Slater-type and numerical orbitals were employed, London dispersion interactions were included, following Grimme's D3 approach.[7] The geometries were fully optimized using 1D and 2D periodic models for edge (e-FeN_4(A) and e-FeN_4(Z)) and basal-plane (b-FeN_4) models, respectively. No relativistic effects and no frozen core were applied. Spin-polarized DFT calculations were performed for the oxygen-containing intermediates, i.e., OOH*, O*, and OH*.

The ORR performance was explored under the theoretical framework developed by Nørskov et al.[8] Here, the associative mechanism and a four-electron pathway was considered, according to which the ORR elementary reactions are described as follows:

$$O_2(g) + {}^* \rightarrow O_2^* \quad (8)$$

$$O_2^* + H^+ + e^- \rightarrow OOH^* \quad (9)$$

$$OOH^* + H^+ + e^- \rightarrow O^* + H_2O(l) \quad (10)$$

$$O^* + H^+ + e^- \rightarrow OH^* \quad (11)$$

$$OH^* + H^+ + e^- \rightarrow * + H_2O(l) \quad (12)$$

where * represents an active site. OOH*, O*, and OH* are the active sites with OOH, O, and OH intermediate adsorption, respectively. The free energy of the intermediates is defined as:

$$\Delta G = \Delta E + \Delta ZPE - T\Delta S + \Delta G_{pH} + \Delta G_U \quad (13)$$

where ΔE is the reaction energy of each step, obtained from DFT calculations; ΔZEP is the change of zero-point energies in the reactions; $T\Delta S$ is the entropy contribution at 300 K; ΔG_{pH} is the correction of H^+ concentration. In this work, we considered the acidic condition, meaning that ΔG_{pH} was taken as zero. ΔG_U is the influence of applied potential, defined as: ΔG_U = -eU, where U is the potential at the electrode and e is the transferred charge. For the small difference between the vibrational frequencies of the adsorbents on the surface, the ΔZPE and $T\Delta S$ were taken from the previous work[9].The overpotential η for ORR is evaluated as:

$$\eta = 1.23 - \frac{\min\left(\Delta G_1, \Delta G_2, \Delta G_3, \Delta G_4\right)}{e} \quad (14)$$

where ΔG_i (i = 1-4) is the free energy of reactions (9) to (12).

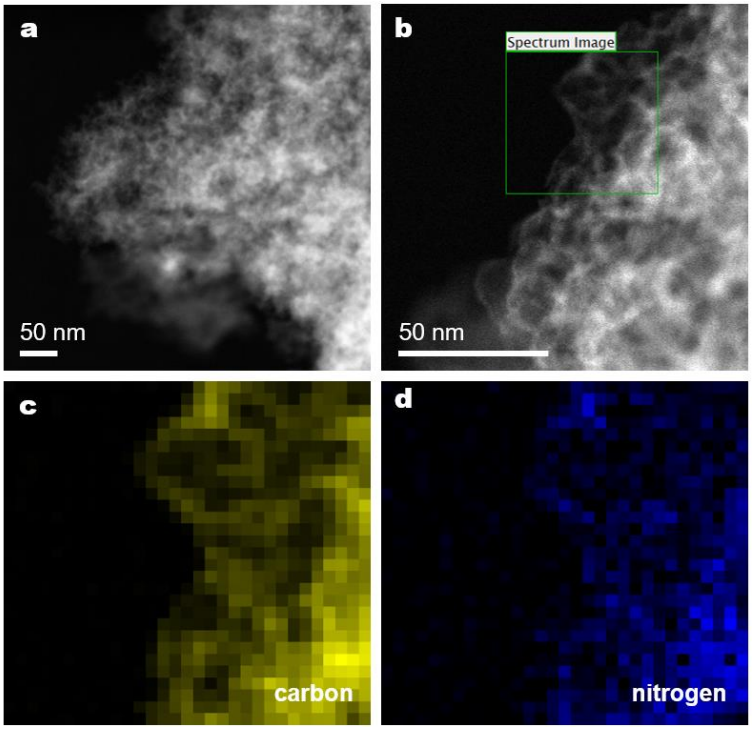

Fig. S1. (a) HAADF-STEM image. (b) HAADF-STEM and corresponding elemental mapping images showing the distribution of (c) carbon and (d) nitrogen elements for NHPC.

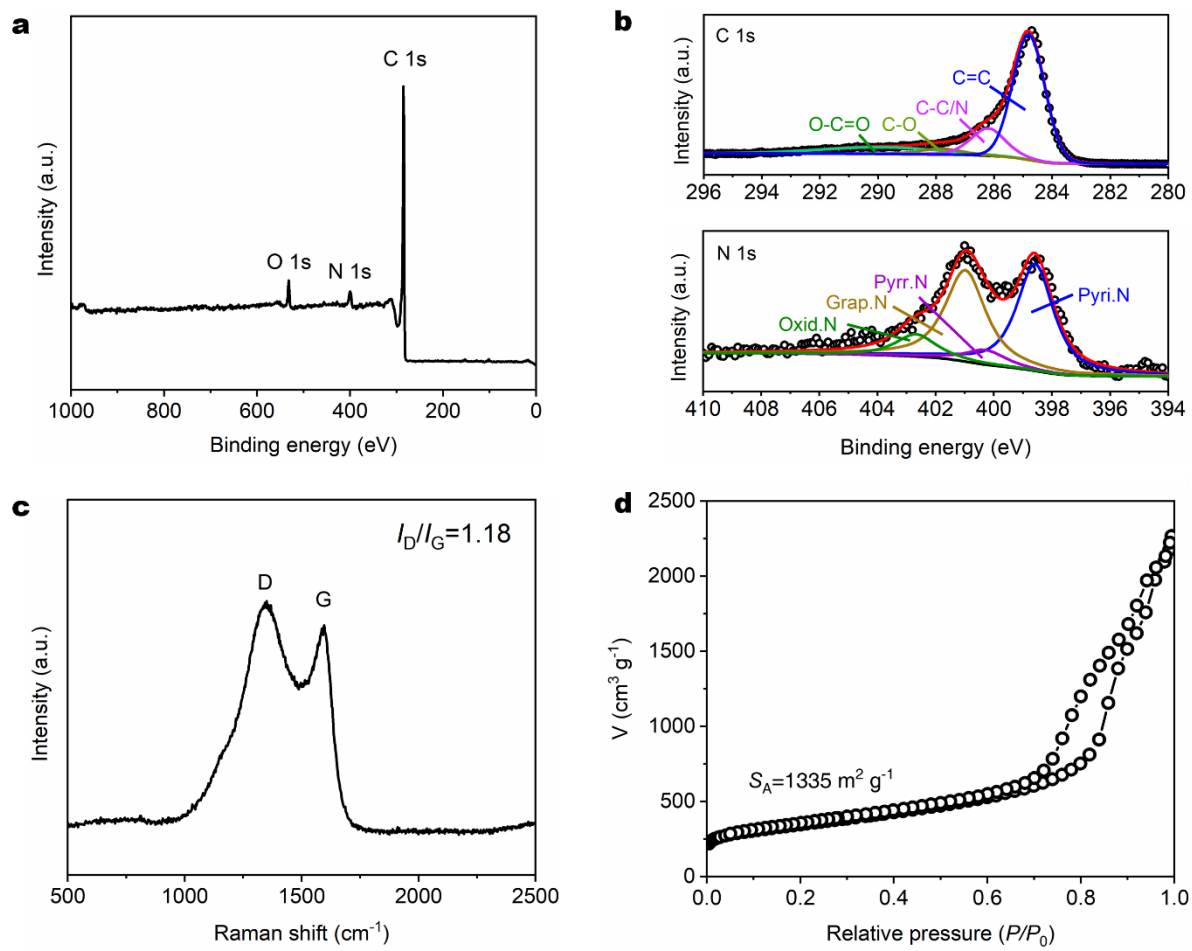

Fig. S2. (a) XPS survey spectrum. (b) High-resolution C 1s and N 1s XPS spectra. (c) Raman spectrum. (d) N_2 adsorption/desorption isotherms of NHPC. The survey spectrum of NHPC confirms the existence of C and N. The high-resolution C 1s spectrum of NHPC displays four peaks at 289.8, 287.8, 286.2, and 284.8 eV, which can be assigned to C=O, C-O, C-C/N, and C=C group, respectively.[10] The high-resolution N 1s spectrum of NHPC was deconvoluted into four types of N species, corresponding to pyridinic N (398.5 eV), pyrrolic N (400.3 eV), graphitic N (401.0 eV), and oxidized N (402.7 eV), respectively.[11] The high I_D/I_G ratio (1.18) in the Raman spectrum of NHPC indicates the existence of abundant defects in the carbon support. The specific surface area of NHPC was measured to be 1335 m^2 g^{-1}. The large surface area of NHPC with abundant surface anchoring sites (e.g., defects, N sites) will efficiently coordinate Fe ions.

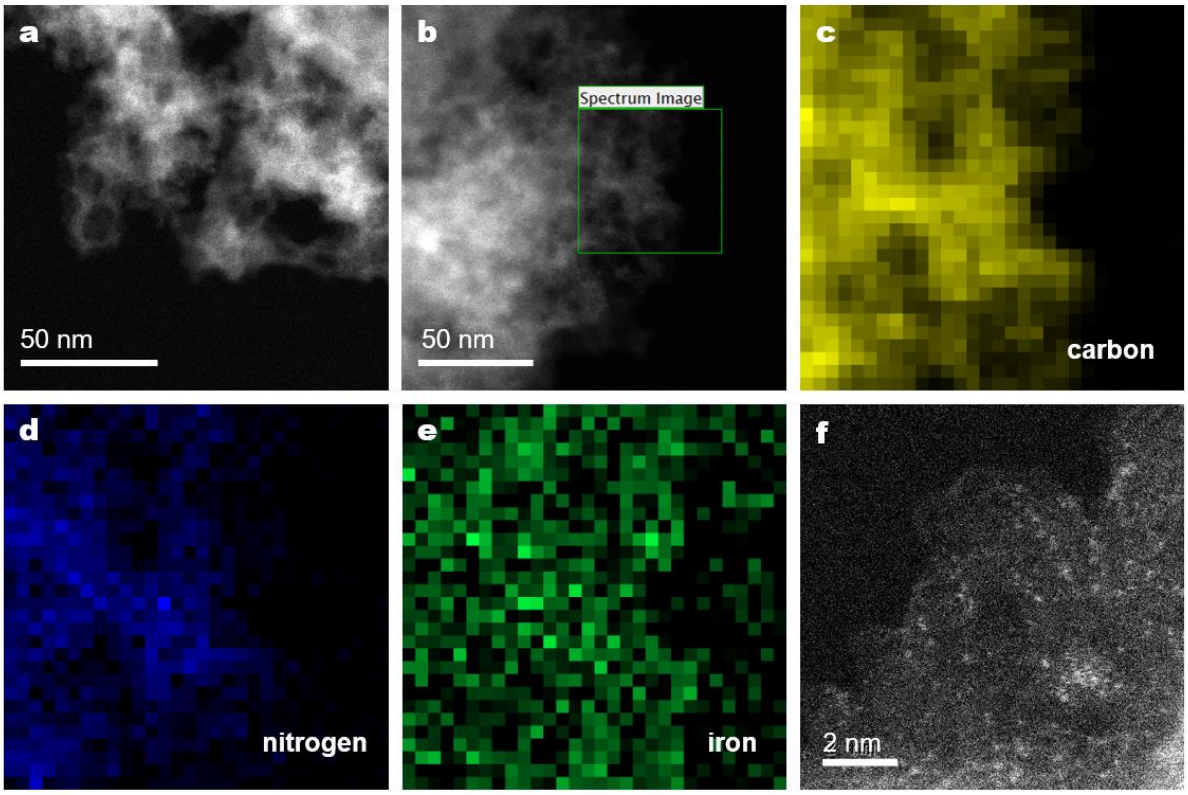

Fig. S3. Characterizations of FeN_4-HPC. (a) HAADF-STEM image. (b) HAADF-STEM and corresponding elemental mapping images showing the distribution of (c) carbon, (d) nitrogen, and (e) iron elements. (f) Atomic-resolution HAADF-STEM image. The bright dots in (f) present the single iron atoms. Clearly, almost all the single iron atoms are located on the basal plane of the carbon support.

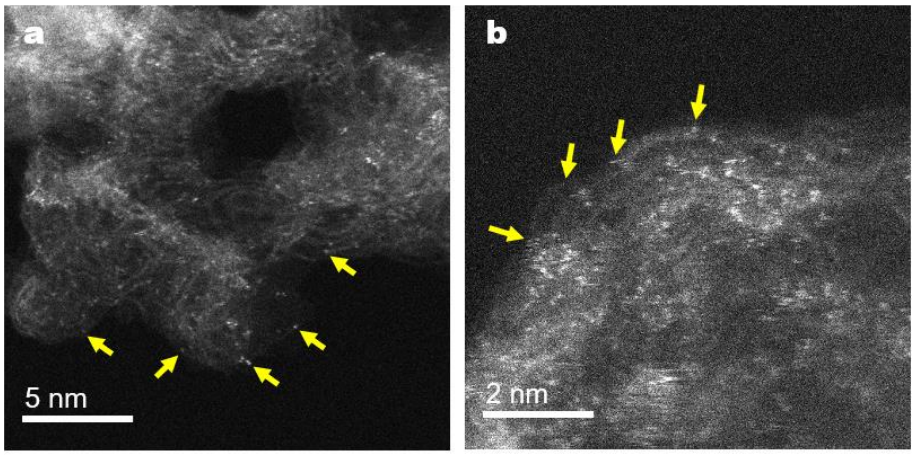

Fig. S4. Atomic-resolution HAADF-STEM images of *sur*-FeN_4-HPC at different locations.

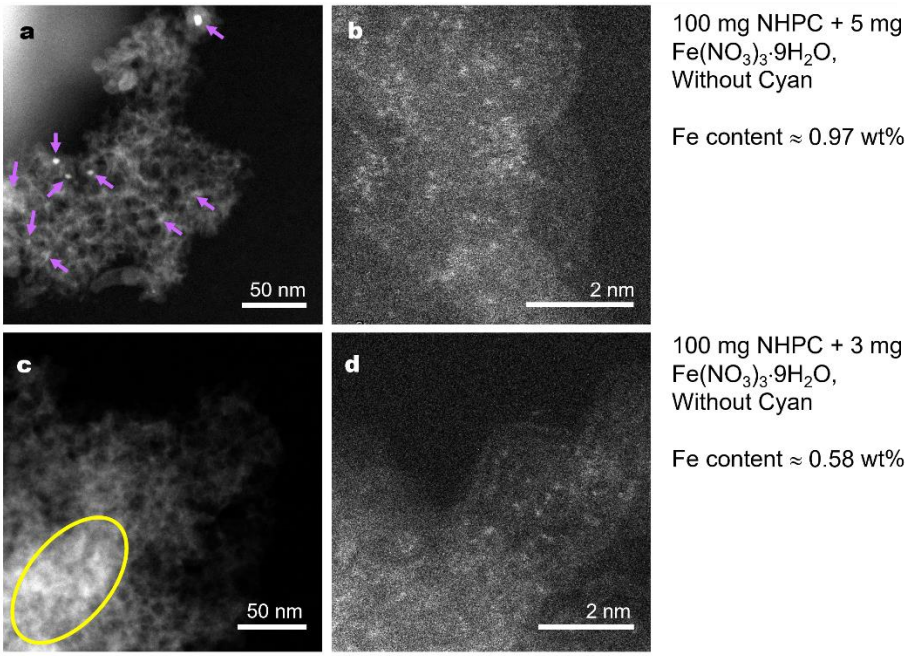

Fig. S5. (a) HAADF-STEM and (b) atomic resolution HAADF-STEM images Fe(5)-HPC-no cyan). The purple arrows in Fig. S5a indicate the formed Fe-nanoparticles. (c) HAADF-STEM and (d) atomic resolution HAADF-STEM denoted as Fe(3)-HPC-no cyan. The bright area seen in Fig. S5c is due to the contrast difference in 3D carbons.

In order to investigate the origination of N in FeN_4, we firstly synthesized Fe(5)-HPC-no cyan by pyrolysis of the mixture of 100 mg NHPC and 5 mg $Fe(NO_3)_3{\cdot}9H_2O$. As shown in **Fig. S5**a, when no cyan was used, Fe-based nanoparticles were detected on the carbon support. Meanwhile, single Fe atoms were also identified in the atomic-resolution HAADF-STEM image (Fig. S5b). The results implied that Fe-nanoparticles and single Fe atoms co-existed on the Fe(5)-HPC-no cyan. The iron content was determined as 0.97 wt% using ICP-OES. We further prepared Fe(3)-HPC-no cyan by pyrolysis of the mixture of 100 mg NHPC and a lower amount of Fe source (i.e., 3 mg $Fe(NO_3)_3{\cdot}9H_2O$). As depicted in Fig. S3c, d, no Fe-nanoparticles were observed on Fe(3)-HPC-no cyan, indicating that the nitrogen from NHPC could also participate in the formation of FeN_4 sites. The Fe content in Fe(3)-HPC-no cyan was determined as low as 0.58 wt%. Besides, on Fe(3)-HPC-no cyan, almost all the single iron atoms are located on the basal plane of the carbon support (Fig. S5d).

These results, together with the characterization results from *sur*-FeN_4-HPC, indicated that the cyan played a significant role in the generation of a higher density of single Fe atoms on *sur*-FeN_4-HPC. The N sites from NHPC will coordinate limited Fe ions, thus resulting in the formation of Fe-nanoparticles on Fe(5)-HPC-no cyan (higher Fe source) and single Fe atoms on Fe(5)-HPC-no cyan (lower Fe source). In *sur*-FeN_4-HPC, the cyan could further provide the nitrogen species for trapping Fe atoms on HPC. Thus, we believe that the N in FeN_4 moieties was derived from both NHPC and cyan. Without the addiction of cyan, it could only provide a single atom Fe-N-C with lower Fe content (e.g., less than 0.6 wt%).

Our previous work indicated that the higher N content in DAP precursor (N/C=3/5) could result in a higher N content in the generated carbon.[12] Thus, in this work, we used DAP as the

N precursor for the fabrication of NHPC. In the second pyrolysis step, we also proved that the cyan has a higher ability than phenanthroline, dipicolylamine and melamine to stabilize single metal atoms, probably due to its size and unique C≡N structures.[13] Thus, we chose DAP and cyan as the corresponding N-containing precursors.

Overall, according to the above results, it is demonstrated that the Fe^{3+} was firstly adsorbed on the surface of NHPC. After the pyrolysis, the Fe^{3+} was transformed to single atoms and then coordinated with pyridinic N on NHPC, forming FeN_4 site. If no cyan was added, not enough pyridinic N was used to coordinate Fe atoms and excessive Fe^{3+} will be reduced for the generation of Fe-nanoparticles. If cyan was added, The C≡N structures in cyan decomposed at the elevated temperature and easily bonded to unsaturated carbon atoms to form stable pyridinic-N,[13] favoring the formation of additional FeN_4 active sites. Thus, the dense single metal FeN_4 moieties can be obtained by simple Fe-ion anchoring and subsequent high-temperature pyrolysis strategy.

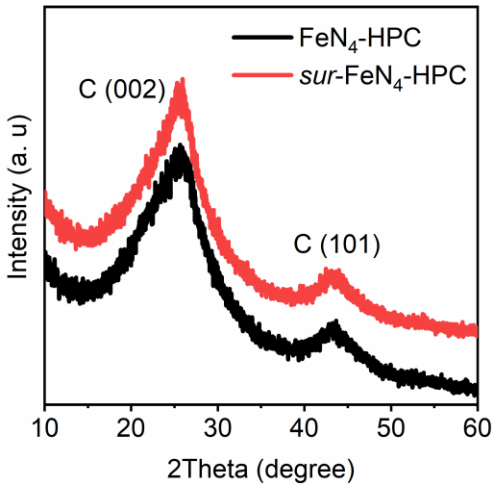

Fig. S6. XRD patterns of FeN_4-HPC and *sur*-FeN_4-HPC.

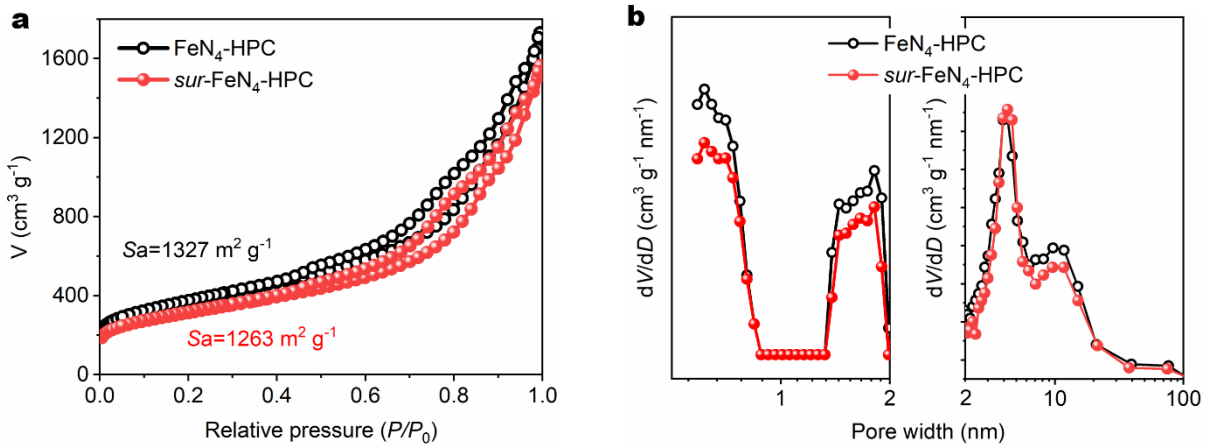

Fig. S7. (a) N_2 adsorption/desorption isotherms of FeN_4-HPC and *sur*-FeN_4-HPC. (b) The corresponding pore size distribution curves calculated from the adsorption branches. Nitrogen-sorption analysis was employed to examine the porous properties of the *sur*-FeN_4-HPC and FeN_4-HPC electrocatalysts. As shown in Fig. S6, both *sur*-FeN_4-HPC and FeN_4-HPC displayed a steep increase in V_{ads} at a relatively low N_2 pressure (P/P_0 = 0-0.015) and a well-defined hysteresis loop at a higher N_2 pressure (P/P_0 = 0.4-0.95), suggesting the coexistence of micropores and mesopores.[14] The Brunauer-Emmett-Teller (BET) surface area and the total pore volume of *sur*-FeN_4-HPC were measured to be 1263 m^2 g^{-1} and 2.5 cm^3 g^{-1}, which were comparable to 1327 m^2 g^{-1} and 2.7 cm^3 g^{-1} for FeN_4-HPC.

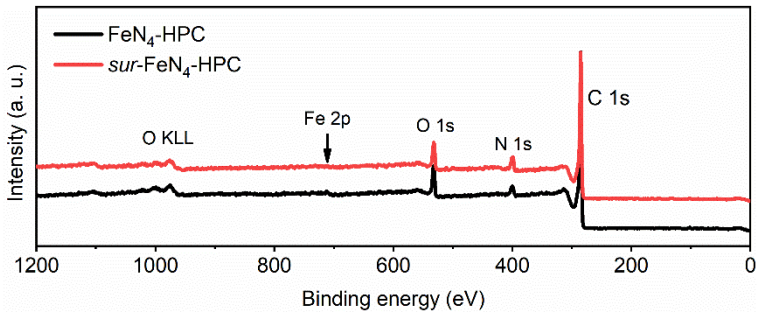

Fig. S8. XPS survey spectra of FeN_4-HPC and *sur*-FeN_4-HPC, showing the presence of C, N, Fe and O peaks. The weak intensities of Fe 2p peaks are due to the low single iron loadings (< 1.3 wt%).

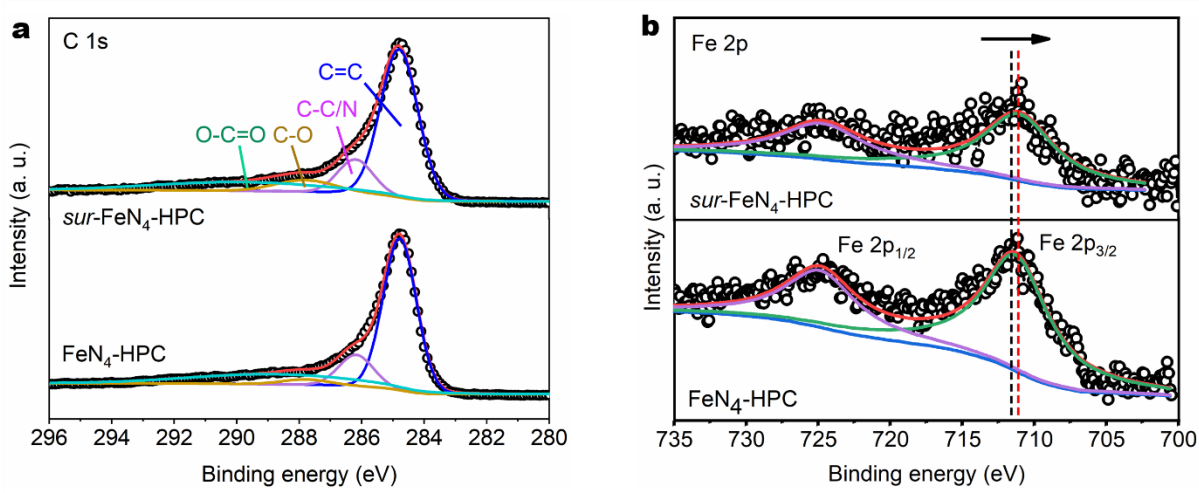

Fig. S9. High-resolution (a) C 1s XPS spectra and (b) Fe 2p XPS spectra of FeN_4-HPC and *sur*-FeN_4-HPC. The high-resolution C 1s spectrum of *sur*-FeN_4-HPC displays four peaks at 289.8, 287.8, 286.2, and 284.8 eV, which can be assigned to C=O, C-O, C-C/N, and C=C group, respectively.[10]

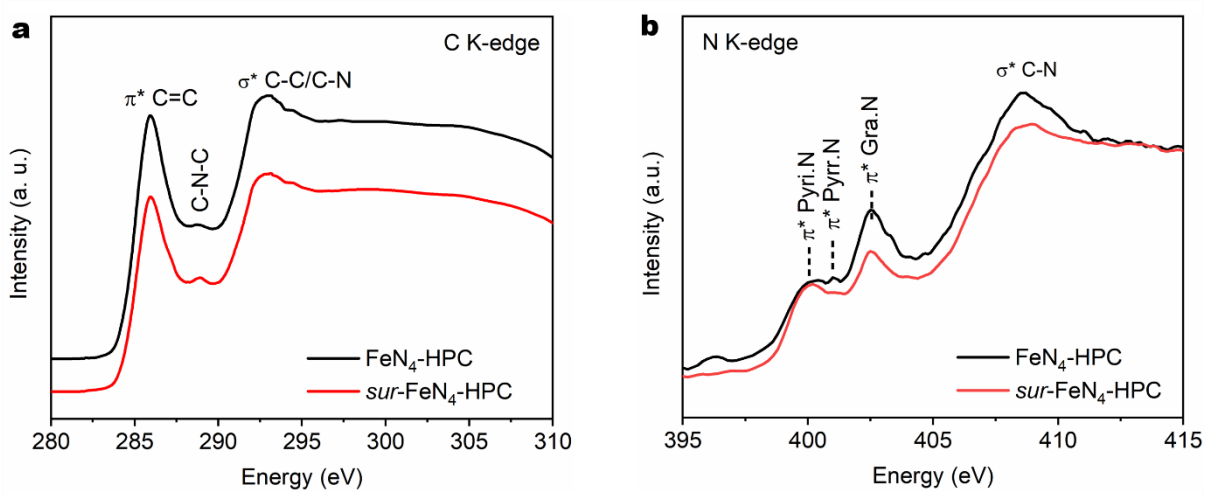

Fig. S10. (a) C K-edge XANES spectra of FeN_4-HPC and *sur*-FeN_4-HPC. The peaks observed at ~285.9 eV and ~293.0 eV is attributed to C=C π* transition and C-C σ* transitions, respectively. The peak at ~288.8 eV suggests the formation of C-N-C. (b) N K-edge XANES spectra of FeN_4-HPC and *sur*-FeN_4-HPC. For the N K-edge XANES spectra, three obvious peaks were observed at 400.1, 402.5, and 408.4 eV, which corresponded to a π*-transition of the pyridinic N sites, π*-transition of the graphitic N sites, and σ*-transition of the C-N bonds, respectively.[15]

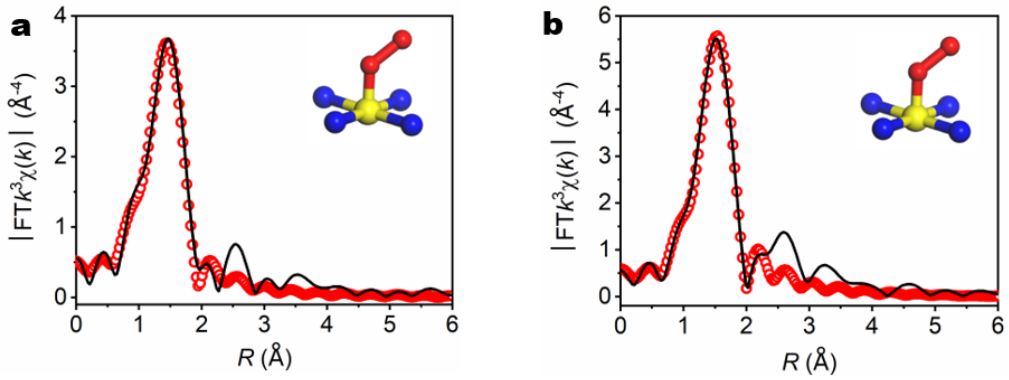

Fig. S11. Fe K-edge EXAFS fitting results of (a) FeN_4-HPC and (b) *sur*-FeN_4-HPC. The fitting parameters and results are given in Table S1. The first coordination shell of *sur*-FeN_4-HPC could be fitted by a mixture of Fe-N and Fe-O coordination paths, with coordination numbers (*CN*) of 4.1 ± 0.4 and 1.0 ± 0.1, respectively. This suggests that the central Fe site in the *sur*-FeN_4-HPC possessed a FeN_4O configuration, i.e., a plane FeN_4 moiety with one axial oxygen atom. The O path was probably due to the adsorption of O_2 from the air.[16]

Table S1. Fe K-edge EXAFS fitting results of Fe foil, FeN_4-HPC and *sur*-FeN_4-HPC.

Sample	**Path**	***N***	***R* (Å)**	**σ^2 ($\times10^{-3}$ Å^2)**	**ΔE_0 (eV)**	***R*, %**
Fe foil[a]	Fe-Fe1	**8.0**	2.46±0.02	5±2	4.3±2.2	0.67
	Fe-Fe2	**6.0**	2.84±0.01	5±2		
FeN_4-HPC[b]	Fe-N	3.8±0.5	2.01±0.06	10±8	-2.4±1.3	0.42
	Fe-O	0.9±0.1	1.93±0.18			
sur-FeN_4-HPC[c]	Fe-N	4.1±0.4	2.03±0.02	Fe-N	1.3±0.8	0.20
	Fe-O	1.0±0.1	1.93±0.14	Fe-O		

[a]: *k* range: 2.3-11.1 (Å^{-1}); *R* range: 1.0-2.9 Å; [b]: *k* range: 2.5-10 (Å^{-1}); *R* range: 1.0-2.3 Å; [c]: *k* range: 2.5-10 (Å^{-1}); *R* range: 1-2.3 Å; S_0^2 = 0.69, S_0^2 is determined from Fe foil. The bold numbers were set as fixed coordination numbers.

Table S2. ORR performance comparison of *sur*-FeN_4-HPC and reported state-of-the-art Fe-N-C electrocatalysts in acidic electrolytes.

Catalyst	**$E_{1/2}$ (V *vs.* RHE)**	**Electrolyte**	**Reference**
sur-FeN_4-HPC	0.83	0.1 M $HClO_4$	This work
FeN_4-HPC	0.76	0.1 M $HClO_4$	This work
(CM+PANI)-Fe-C	0.80	0.5 M H_2SO_4	*Science* 2017, **357**, 479-484.[17]
Fe-ZIF	0.85	0.5 M H_2SO_4	*J. Am. Chem. Soc.* 2017, **139**, 14143.[18]
Fe/SNC	0.77	0.5 M H_2SO_4	*Angew. Chem. Int. Ed.* 2017, **56**, 13800.[19]
SA-Fe/NG	0.8	0.5 M H_2SO_4	*Proc. Natl. Acad. Sci.* 2018, **115**, 6626.[20]
SA-Fe-HPC	0.81	0.1 M $HClO_4$	*Angew. Chem. Int. Ed.* 2018, **57**,9038.[21]
Fe-SAs/NPS-HC	0.791	0.5 M H_2SO_4	*Nat Commun.* 2018, **9**, 5422.[22]
TPI@Z8(SiO_2)-650-C	0.82	0.5 M H_2SO_4	*Nat. Catal.* 2019, **2**, 259-268.[23]
p-Fe-N-CNFs	0.74	0.1 M $HClO_4$	*Energy Environ. Sci.* 2018, **11**, 2208-2215.[24]
Fe-N-C-950	0.78	0.1 M $HClO_4$	*ACS Catal.* 2018, **8**, 2824-2832.[25]
SA-Fe-N NS	0.81	0.5 M H_2SO_4	*Adv. Energy Mater.* 2018, **8**, 1801226.[26]
Fe2-Z8-C	0.805	0.5 M H_2SO_4	*Angew. Chem. Int. Ed.* 2018, **57**, 1204-1208.[27]
Fe SAs/N-C	0.798	0.1 M $HClO_4$	*ACS Catal.* 2019, **9**, 2158-2163.[28]
Fe-N_4-C-60	0.8	0.1 M $HClO_4$	*Adv. Mater.* 2020, **32**, 2000966.[29]
Fe2-N-C	0.78	0.5 M H_2SO_4	*Chem* 2019, **5**, 2865-2878.[30]
Fe-C-N950	0.8	0.1 M $HClO_4$	*J. Am. Chem. Soc.* 2020, **142**, 5477-5481.[31]
$Fe_1(II)-N_4$	0.8	0.1 M $HClO_4$	*J. Am. Chem. Soc.* 2020, **142**, 1417-1423.[32]
Fe/OES	~0.7	0.5 M H_2SO_4	*Angew. Chem. Int. Ed.* 2020, **59**, 7384-7389.[33]
ZIF-NC-0.5Fe-700	0.84	0.5 M H_2SO_4	*Angew. Chem. Int. Ed.* 2019, **58**, 18971-18980.[34]
HP FeN_4	0.80	0.5 M H_2SO_4	*Energy Environ. Sci.* 2020, **13**, 111-118.[35]
FeN_4/HOPC-c-1000	0.80	0.5 M H_2SO_4	*Angew. Chem. Int. Ed.* 2020, **59**, 2688-2694.[36]

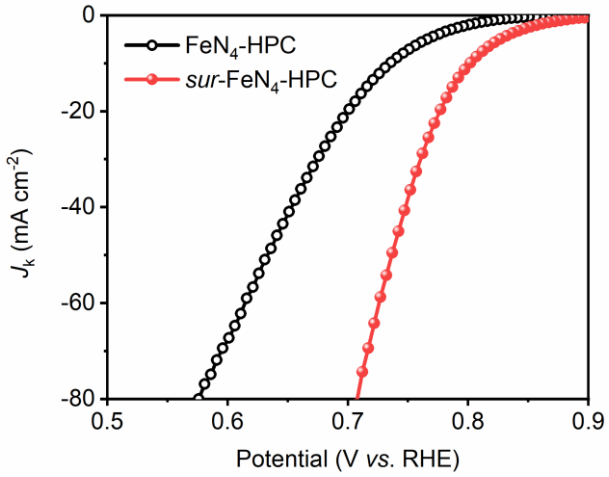

Fig. S12. Kinetic current density curves of FeN_4-HPC and *sur*-FeN_4-HPC.

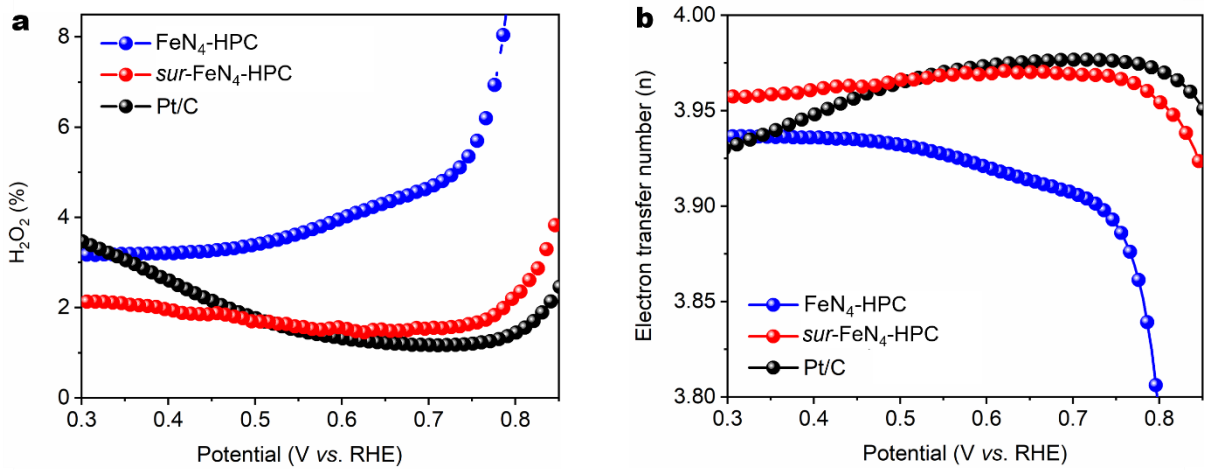

Fig. S13. (a) H_2O_2 yield and (b) electron transfer number plots of FeN_4-HPC, *sur*-FeN_4-HPC and Pt/C electrocatalysts.

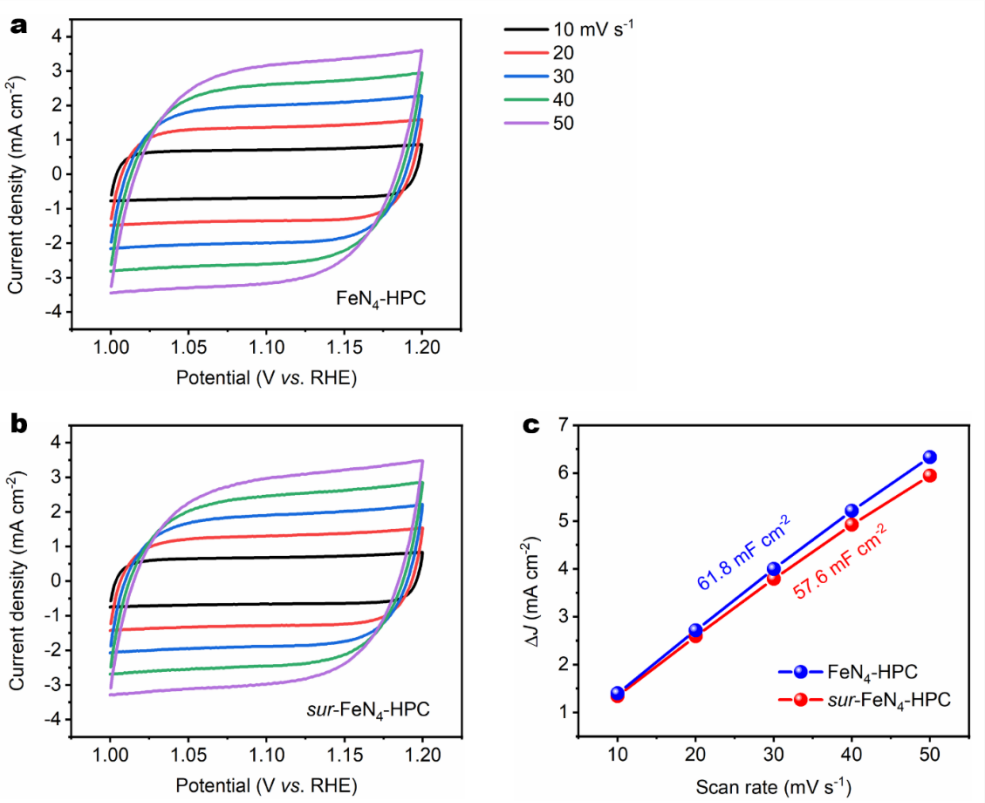

Fig. S14. CV curves collected at different scan rates for (a) FeN_4-HPC and (b) *sur*-FeN_4-HPC. (c) Charge current density differences (ΔJ) at 1.10 V (vs. RHE) for FeN_4-HPC and *sur*-FeN_4-HPC plotted against scan rate.

The electrochemically active surface areas (ECSA) were studied based on the electrochemical double-layer capacitance of the electrocatalysts at non-faradaic overpotentials. By plotting the difference of current density (J) between the anodic and cathodic sweeps ($J_{anodic} - J_{cathodic}$) at 1.10 V *vs*. RHE against the scan rate (ν), a linear trend was observed. The slope of the fitting line is equal to twice the geometric double layer capacitance (C_{dl}), which is proportional to the effective electrode surface area of the materials. As disclosed in Fig. S14, the *C*dl of *sur*-FeN_4-HPC was calculated to be 57.6 mF cm^{-2}, which was slightly smaller than 61.8 mF cm^{-2} for FeN_4-HPC.

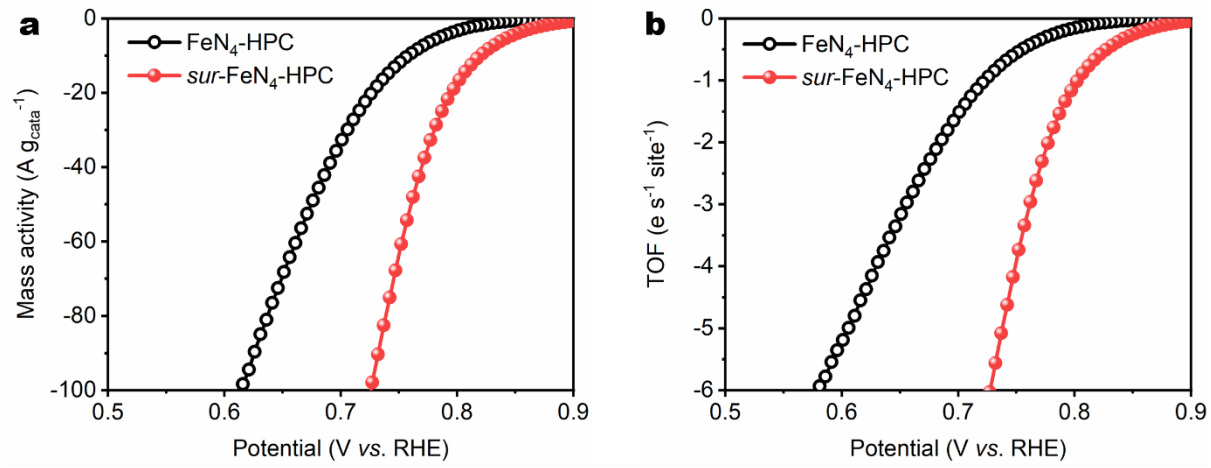

Fig. S15. (a) Mass activity and (b) TOF curves of FeN_4-HPC and *sur*-FeN_4-HPC catalysts. Fig. S15b displayed the apparent TOF curves, where we assumed that all the Fe sites participated in the ORR process. The intrinsic TOF will be determined according to the accessibility of the FeN_4 sites.

Table S3. ORR mass activity comparison of *sur*-FeN_4-HPC and reported state-of-the-art Fe-N-C electrocatalysts.

Catalyst	**Electrolyte**	**Mass activity at 0.8 V *vs.* RHE (A g^{-1})**	**Reference**
sur-FeN_4-HPC	0.1 M $HClO_4$	16.5	This work
(CM+PANI)- Fe-C	0.5 M H_2SO_4	2.5	*Science* 2017, **357**, 479-484.[17]
SA-Fe/NG	0.5 M H_2SO_4	4.3	*Proc. Natl. Acad. Sci. USA* 2018, **115**, 6626-6631.[20]
TPI@Z8(SiO_2)-650-C	0.5 M H_2SO_4	9.3	*Nat. Catal.* 2019, **2**, 259-268.[23]
Fe_2-N-C	0.5 M H_2SO_4	6.3	*Chem* 2019, **5**, 2865-2878.[30]
Fe_2N_6	0.5 M H_2SO_4	8.48	*Matter* 2020, **3**, 509-521.[37]

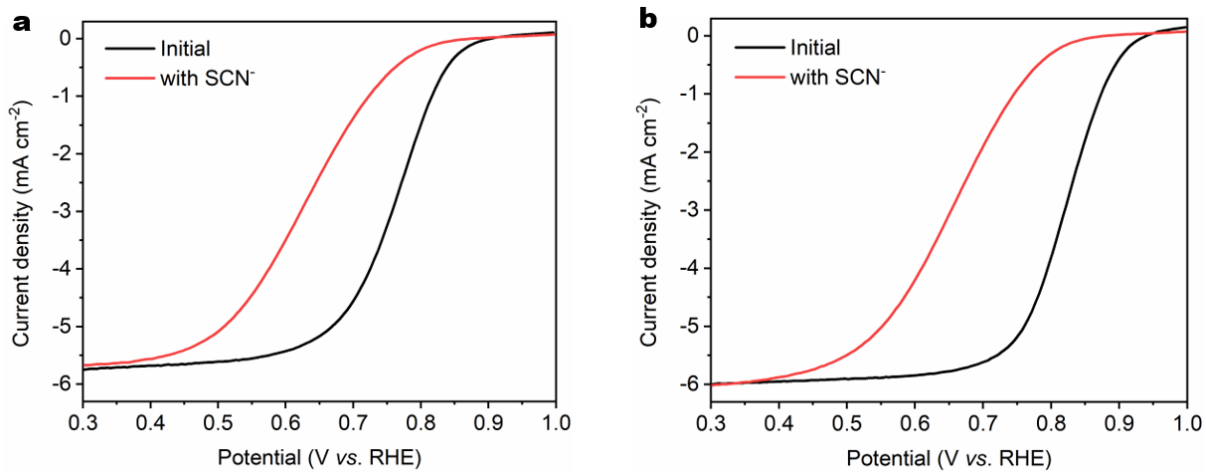

Fig. S16. Identification of the active sites. Effects of SCN ions (20 mM) on the ORR activities of (a) FeN_4-HPC and (b) *sur*-FeN_4-HPC in a 0.1 M $HClO_4$ electrolyte solution. To understand the nature of the active sites, poisoning experiments of thiocyanate ions (SCN^-) on the ORR activity were carried out as SCN^- is widely known to poison Fe sites under acidic conditions.[38] Upon introducing 20 mM SCN^-, the $E_{1/2}$ of FeN_4-HPC and *sur*-FeN_4-HPC negatively shifted by ~120 mV and ~170 mV, uncovering that the atomic Fe sites were the real active sites for catalysing the ORR kinetics.

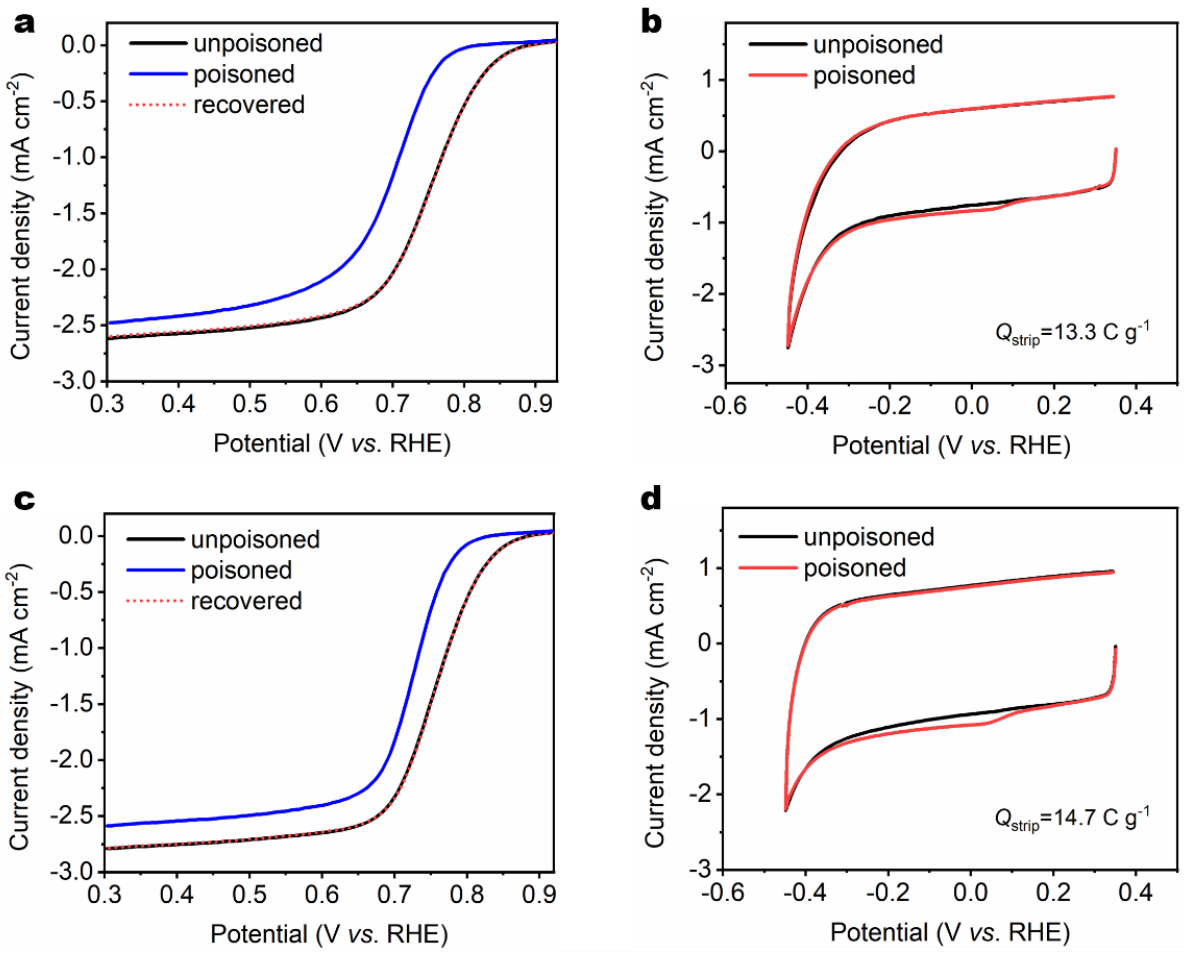

Fig. S17. Determination of the accessible FeN4 site density (SD) for (a, b) FeN_4-HPC and c, d) *sur*-FeN_4-HPC. (a) and (c) ORR LSV curves before, during and after nitrite adsorption in an O2-saturated 0.5 M acetate buffer at pH 5.2. (b) and (d) CV curves before and during nitrite adsorption in the nitrite reductive stripping region. Catalyst loading: 270 µg cm^{-2}.

Table S4. Intrinsic TOF value comparison of *sur*-FeN_4-HPC and reported state-of-the-art Fe-N-C catalysts.

Catalyst	**Electrolyte**	**TOF (s^{-1}) at 0.8 V**	**Reference**
sur-FeN_4-HPC	0.1 M $HClO_4$	1.76	This work
FeN_4-HPC	0.1 M $HClO_4$	0.62	This work
0.5Fe-950	0.1 M H_2SO_4	0.33	*Nat. Mater. 2015*, **14**, 937.[39]
CNT/PC	0.1 M $HClO_4$	0.22	*J. Am. Chem. Soc*. 2016, **138**, 15046.[40]
Fe-SA-NSFC	0.1 M $HClO_4$	0.17	*Nat. Commun.* 2020, **11**, 5892.[41]
Fe-N-C-950	0.1 M $HClO_4$	1.71	*ACS Catal.* 2018, **8**, 2824-2832.[25]
FeNC	0.1 M $HClO_4$	0.156	*Nat. Mater.* 2020, **19**, 1215-1223.[42]

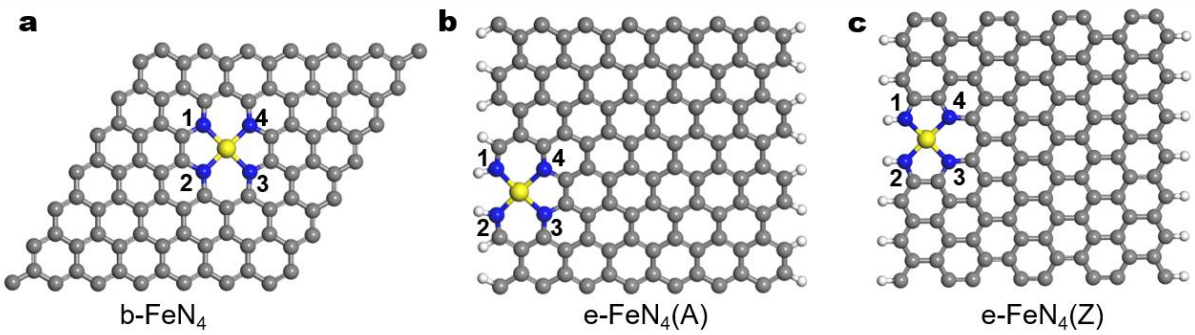

Fig. S18. The as-built structural models of (a) b-FeN_4, (b) e-FeN_4(A), and (c) e-FeN_4(Z). Grey, blue, yellow, and white sphere represents C, N, Fe, and H atoms, respectively.

Table S5. Fe-N bond lengths in b-FeN_4, e-FeN_4(A) and e-FeN_4(Z).

Bond length (Å)	**b-FeN_4**	**e-FeN_4(A)**	**e-FeN_4(Z)**
Fe-N1	1.90	1.88	1.84
Fe-N2	1.90	1.88	1.84
Fe-N3	1.90	1.95	1.91
Fe-N4	1.90	1.95	1.91
Average Fe-N	1.90	1.92	1.88

For e-FeN_4(A), the bond length of Fe-N1, Fe-N2, Fe-N3 and Fe-N4 is 1.88, 1.88, 1.95 and 1.95 Å, respectively, leading an average Fe-N bond length of 1.92 Å in e-FeN_4(A), which is longer than that in b-FeN_4 (1.90 Å). The increased average bond length in e-FeN_4(A) relative to b-FeN_4 is resulting from the edge tensile strain (ETS, with longer Fe-N bond length relative to that of basal-plane carbon) effect on the armchair-edged carbon lattice.[43] The zigzag-edge carbon (e-FeN_4(Z)), on the contrary, has an average Fe-N bond length of 1.88 Å. The reduced average Fe-N bond length in e-FeN_4(Z) is due to the edge compressive strain (ECS, with shorter Fe-N bond length relative to that of basal-plane carbon) effect on the zigzag-edged carbon lattice.[44, 45]

Table S6. Calculated spin moment of Fe center, adsorption energies and Gibbs free energies of oxygen reduction intermediates on each structure.

	b-FeN$_4$	**e-FeN$_4$(A)**	**e-FeN$_4$(Z)**
Spin moment of Fe (μ_B)	1.97	1.84	1.92
ΔE_{OOH*} (eV)	3.03	3.37	2.75
ΔE_{O*} (eV)	1.25	1.54	1.41
ΔE_{OH*} (eV)	0.12	0.54	0.19
ΔG_{OOH*} (eV)	3.43	3.77	3.15
ΔG_{O*} (eV)	1.30	1.59	1.46
ΔG_{OH*} (eV)	0.47	0.89	0.54

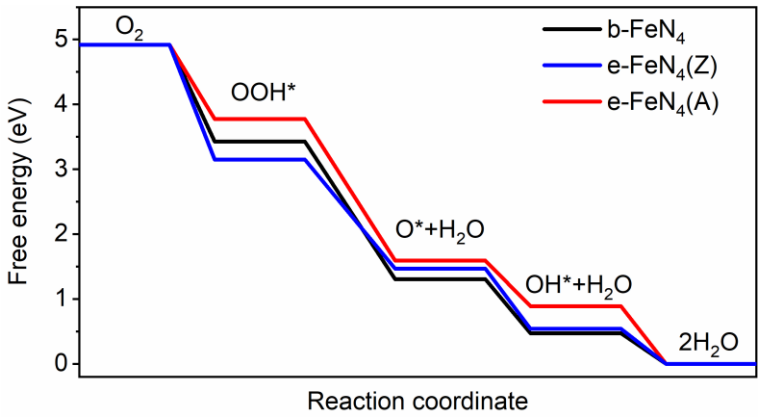

Fig. S19. Free-energy diagrams for ORR under zero potential (U = 0 V) on b-FeN_4, e-FeN_4(Z), and e-FeN_4(A).

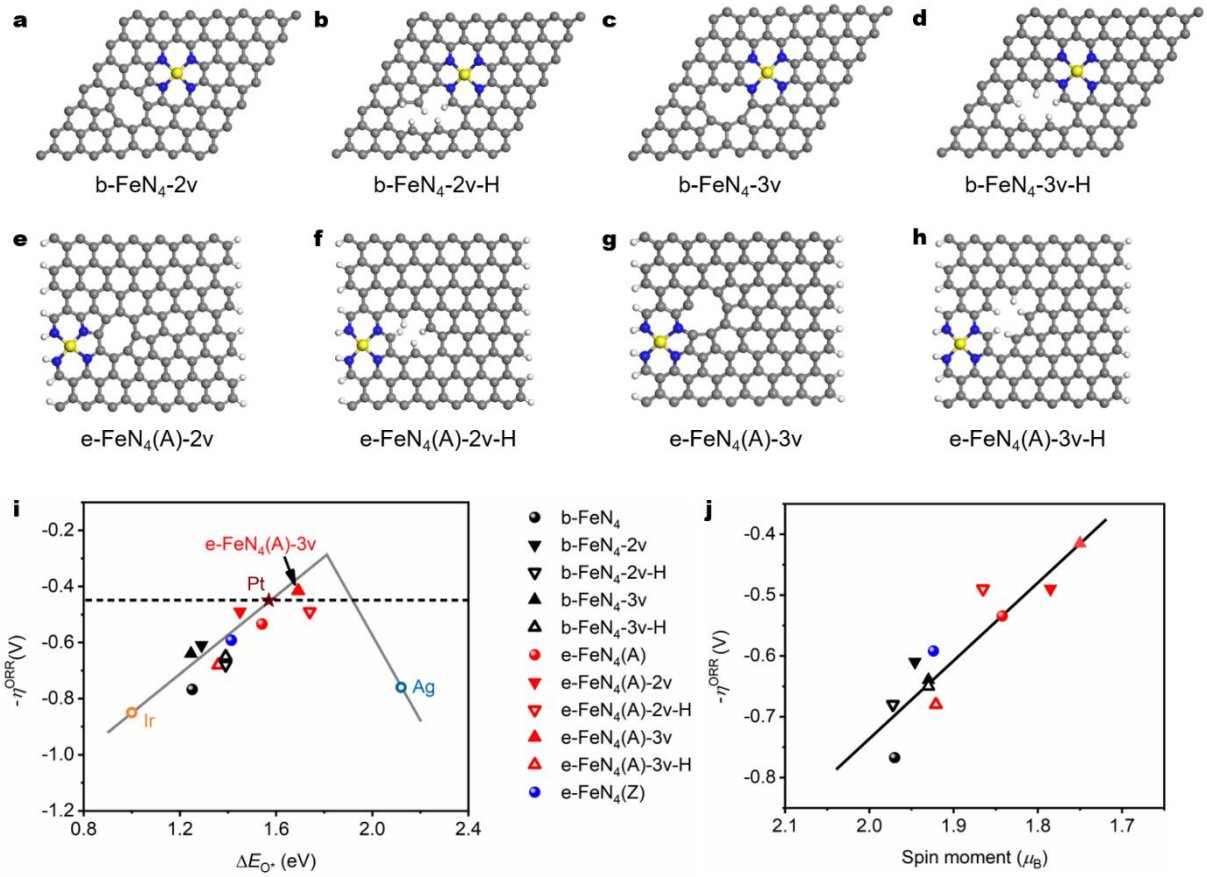

Fig. S20. The influence of lattice defect on ORR activity. As vacancy defects are quite common in experimentally prepared Fe-N-C catalysts, we have also checked the influence of common carbon vacancy defects (2- and 3-atom vacancy) on the ORR activity. Defects are denoted with v; note the formation of such defects is beyond the scope of this work. Defects were either saturated with H atoms or unsaturated and atomic reconstruction was observed after relaxation. The following nomenclature was used: b-FeN_4-nv (e-FeN_4-nv) - unsaturated, and b-FeN_4-nv-H (e-FeN_4-nv-H) - hydrogen saturated, with n being the number of vacancies, here 2 or 3. Models with 2-carbon atom vacancy in the basal plane without (a) and with saturation (b); (c) and (d) the corresponding models for 3-carbon atom vacancy; (e)-(h) corresponding models at the armchair edge. (i) Trends of ORR activity (negative ORR overpotential, $-\eta^{ORR}$) plotted as function of the oxygen-adsorption energy (ΔE_{O*}) on different catalyst models, from which one can see that defects would not reduce the activity on b-FeN_4 and e-FeN_4(A), rather on the contrary, most defective systems also show higher ORR activity. This is due to the binding energy of O*, which is weakened in these cases. The ORR activity of e-FeN_4(A)-3v is even better than the benchmark Pt. (j) The correlation of η^{ORR} and spin moment of the single Fe center in each system. The spin moment of Fe center decreases also in all defective models, resulting with higher ORR activity. Note that detailed investigations of defect formation are beyond the scope of this work.

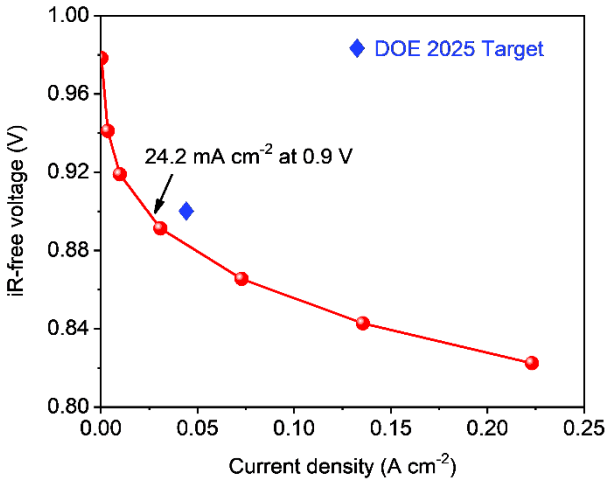

Fig. S21. Polarization curve for determining mass activity of *sur*-FeN_4-HPC cathode at 0.9 $V_{iR\text{-}free}$ measured 1.0 bar H_2-O_2 conditions.

Table S7. PEMFC performance comparison of *sur*-FeN_4-HPC and reported state-of-the-art Fe-N-C electrocatalysts.

Catalyst	1.0 bar H_2-O_2 cell		1.0 bar H_2-air cell		Reference
	j **at 0.9** $V_{iR\text{-}free}$[a]	P_{max}[b]	***j*** **at 0.65 V**[a]	P_{max}[b]	
sur-FeN_4-HPC	24.2	0.79	449	0.412	This work
FeN_4-HPC	13.4	0.43	211	0.265	This work
PANI-FeCo-C	-	0.55	-	-	*Science* 2011, **332**, 443-447.[46]
1.5Fe-ZIF	18	0.679	420	0.36	*Energy Environ. Sci.* 2019, **12**, 2548-2558.[47]
ZIF-NC-0.5Fe-700	30	0.73	625	0.29	*Angew. Chem. Int. Ed.* 2019, **58**, 18971-18980.[34]
0.17CVD/Fe-NC-kat	27	0.70	448	0.32	*Angew. Chem. Int. Ed.* 2020, **59**, 21698-21705.[48]
TPI@Z8(SiO_2)-650-C	22	1.18 (2.5 bar)	590	0.42	*Nat. Catal.* 2019, **2**, 259-268.[4]
$FeCl_2$\/NC-1000	15	-	240	0.28	*J. Am. Chem. Soc.* 2020, **142**, 1417-1423.[32]
Fe/TPIZ/ZIF-8	4		425	0.30	*Angew. Chem. Int. Ed.* 2013, **52**, 6867-6870.[49]
Fe SAs/N-C	-	0.75	-	0.35	*ACS Catal.* 2019, **9**, 2158-2163.[28]
Fe-N/CNT-2	-	0.36	-	-	*Adv. Funct. Mater*. 2019, **29**, 1906174.[50]
CM+PANI)-Fe-C	16	0.87	-	0.42	*Science* 2017, **357**, 479-484.[17]
Fe-N_4-C-60	-	0.74	-	-	*Adv. Mater.* 2020, **32**, 2000966.[29]
FePhen@MOF-Ar NH_3	-	-	~380	0.38	*Nat. Commun.* 2015, **6**, 7343 (2015).[51]
Fe_2N_6	-	0.845	-	0.36	*Matter* 2020, **3**, 509-521.[37]

Note: [a] mA cm^{-2}; [b] W cm^{-2}.

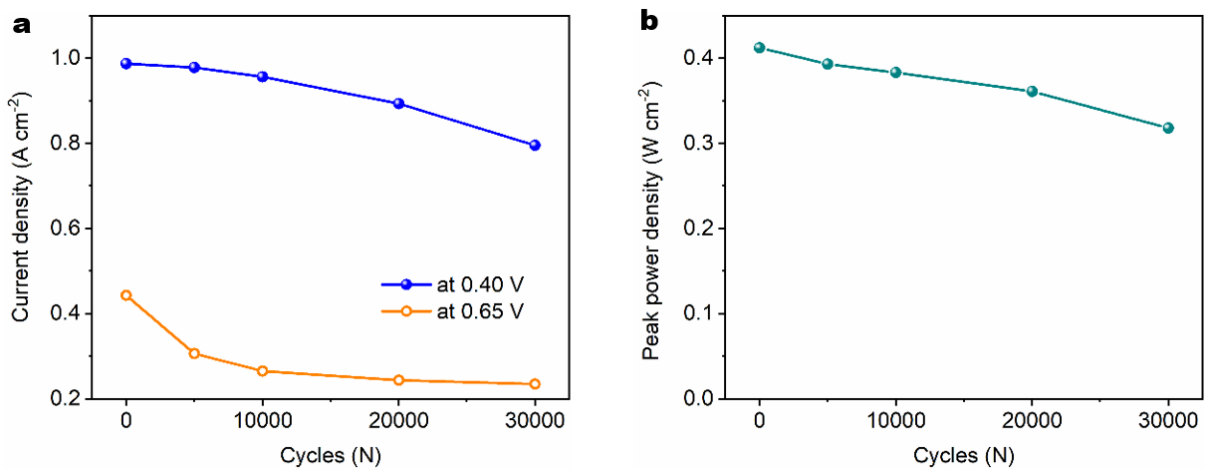

Fig. S22. H_2-air PEMFC stability tests of *sur*-FeN_4-HPC. (a) Current density losses at 0.40 V and 0.65 V. (b) Peak power density loss.

References

1. M. Newville, *J. Synchrotron Rad.*, 2001, **8**, 322-324.
2. M. Zhang, B. Yang, T. Yang, Y. Yang and Z. Xiang, *Chin. Chem. Lett.*, 2022, **33**, 362-367.
3. D. Malko, A. Kucernak and T. Lopes, *Nat Commun*, 2016, **7**, 13285.
4. X. Wan, X. Liu, Y. Li, R. Yu, L. Zheng, W. Yan, H. Wang, M. Xu and J. Shui, *Nature Catalysis*, 2019, **2**, 259-268.
5. G. te Velde, F. M. Bickelhaupt, E. J. Baerends, C. Fonseca Guerra, S. J. A. van Gisbergen, J. G. Snijders and T. Ziegler, *J. Comput. Chem.*, 2001, **22**, 931-967.
6. J. P. Perdew, K. Burke and M. Ernzerhof, *Phys. Rev. Lett.*, 1996, **77**, 3865-3868.
7. S. Grimme, S. Ehrlich and L. Goerigk, *J. Comput. Chem.*, 2011, **32**, 1456-1465.
8. J. K. Nørskov, J. Rossmeisl, A. Logadottir, L. Lindqvist, J. R. Kitchin, T. Bligaard and H. Jónsson, *J. Phys. Chem. B*, 2004, **108**, 17886-17892.
9. J. Rossmeisl, Z.-W. Qu, H. Zhu, G.-J. Kroes and J. K. Nørskov, *J. Electroanal. Chem.*, 2007, **607**, 83-89.
10. Z. Li, Y. Chen, S. Ji, Y. Tang, W. Chen, A. Li, J. Zhao, Y. Xiong, Y. Wu, Y. Gong, T. Yao, W. Liu, L. Zheng, J. Dong, Y. Wang, Z. Zhuang, W. Xing, C.-T. He, C. Peng, W.-C. Cheong, Q. Li, M. Zhang, Z. Chen, N. Fu, X. Gao, W. Zhu, J. Wan, J. Zhang, L. Gu, S. Wei, P. Hu, J. Luo, J. Li, C. Chen, Q. Peng, X. Duan, Y. Huang, X.-M. Chen, D. Wang and Y. Li, *Nat. Chem.*, 2020, **12**, 764-772.
11. Y. Hou, M. Qiu, M. G. Kim, P. Liu, G. Nam, T. Zhang, X. Zhuang, B. Yang, J. Cho, M. Chen, C. Yuan, L. Lei and X. Feng, *Nat. Commun.*, 2019, **10**, 1392.
12. G. Chen, P. Liu, Z. Liao, F. Sun, Y. He, H. Zhong, T. Zhang, E. Zschech, M. Chen, G. Wu, J. Zhang and X. Feng, *Adv. Mater.*, 2020, **32**, 1907399.
13. J. Li, M. Chen, D. A. Cullen, S. Hwang, M. Wang, B. Li, K. Liu, S. Karakalos, M. Lucero, H. Zhang, C. Lei, H. Xu, G. E. Sterbinsky, Z. Feng, D. Su, K. L. More, G. Wang, Z. Wang and G. Wu, *Nat. Catal.*, 2018, **1**, 935-945.
14. H.-W. Liang, X. Zhuang, S. Brüller, X. Feng and K. Müllen, *Nat. Commun.*, 2014, **5**, 4973.
15. Y. Pan, Y. Chen, K. Wu, Z. Chen, S. Liu, X. Cao, W.-C. Cheong, T. Meng, J. Luo, L. Zheng, C. Liu, D. Wang, Q. Peng, J. Li and C. Chen, *Nat. Commun.*, 2019, **10**, 4290.
16. H. Fei, J. Dong, Y. Feng, C. S. Allen, C. Wan, B. Volosskiy, M. Li, Z. Zhao, Y. Wang, H. Sun, P. An, W. Chen, Z. Guo, C. Lee, D. Chen, I. Shakir, M. Liu, T. Hu, Y. Li, A. I. Kirkland, X. Duan and Y. Huang, *Nat. Catal.*, 2018, **1**, 63-72.
17. H. T. Chung, D. A. Cullen, D. Higgins, B. T. Sneed, E. F. Holby, K. L. More and P. Zelenay, *Science*, 2017, **357**, 479-484.
18. H. Zhang, S. Hwang, M. Wang, Z. Feng, S. Karakalos, L. Luo, Z. Qiao, X. Xie, C. Wang, D. Su, Y. Shao and G. Wu, *J. Am. Chem. Soc.*, 2017, **139**, 14143-14149.

19. H. Shen, E. Gracia-Espino, J. Ma, K. Zang, J. Luo, L. Wang, S. Gao, X. Mamat, G. Hu, T. Wagberg and S. Guo, *Angew. Chem. Int. Ed.*, 2017, **56**, 13800-13804.
20. L. Yang, D. Cheng, H. Xu, X. Zeng, X. Wan, J. Shui, Z. Xiang and D. Cao, *Proc. Natl. Acad. Sci. USA*, 2018, **115**, 6626-6631.
21. Z. Zhang, J. Sun, F. Wang and L. Dai, *Angew. Chem. Int. Ed.*, 2018, **57**, 9038-9043.
22. Y. Chen, S. Ji, S. Zhao, W. Chen, J. Dong, W.-C. Cheong, R. Shen, X. Wen, L. Zheng, A. I. Rykov, S. Cai, H. Tang, Z. Zhuang, C. Chen, Q. Peng, D. Wang and Y. Li, *Nat. Commun.*, 2018, **9**, 5422.
23. X. Wan, X. Liu, Y. Li, R. Yu, L. Zheng, W. Yan, H. Wang, M. Xu and J. Shui, *Nat. Catal.*, 2019, **2**, 259-268.
24. B.-C. Hu, Z.-Y. Wu, S.-Q. Chu, H.-W. Zhu, H.-W. Liang, J. Zhang and S.-H. Yu, *Energy Environ. Sci.*, 2018, **11**, 2208-2215.
25. M. Xiao, J. Zhu, L. Ma, Z. Jin, J. Ge, X. Deng, Y. Hou, Q. He, J. Li, Q. Jia, S. Mukerjee, R. Yang, Z. Jiang, D. Su, C. Liu and W. Xing, *ACS Catal.*, 2018, **8**, 2824-2832.
26. Z. Miao, X. Wang, M.-C. Tsai, Q. Jin, J. Liang, F. Ma, T. Wang, S. Zheng, B.-J. Hwang, Y. Huang, S. Guo and Q. Li, *Adv. Energy Mater.*, 2018, **8**, 1801226.
27. Q. Liu, X. Liu, L. Zheng and J. Shui, *Angew. Chem. Int. Ed.*, 2018, **57**, 1204-1208.
28. Z. Yang, Y. Wang, M. Zhu, Z. Li, W. Chen, W. Wei, T. Yuan, Y. Qu, Q. Xu, C. Zhao, X. Wang, P. Li, Y. Li, Y. Wu and Y. Li, *ACS Catal.*, 2019, **9**, 2158-2163.
29. X. Wang, Y. Jia, X. Mao, D. Liu, W. He, J. Li, J. Liu, X. Yan, J. Chen, L. Song, A. Du and X. Yao, *Adv. Mater.*, 2020, **32**, 2000966.
30. W. Ye, S. Chen, Y. Lin, L. Yang, S. Chen, X. Zheng, Z. Qi, C. Wang, R. Long, M. Chen, J. Zhu, P. Gao, L. Song, J. Jiang and Y. Xiong, *Chem*, 2019, **5**, 2865-2878.
31. T. Al-Zoubi, Y. Zhou, X. Yin, B. Janicek, C. Sun, C. E. Schulz, X. Zhang, A. A. Gewirth, P. Huang, P. Zelenay and H. Yang, *J. Am. Chem. Soc.*, 2020, **142**, 5477-5481.
32. J. Li, L. Jiao, E. Wegener, L. L. Richard, E. Liu, A. Zitolo, M. T. Sougrati, S. Mukerjee, Z. Zhao, Y. Huang, F. Yang, S. Zhong, H. Xu, A. J. Kropf, F. Jaouen, D. J. Myers and Q. Jia, *J. Am. Chem. Soc.*, 2020, **142**, 1417-1423.
33. C.-C. Hou, L. Zou, L. Sun, K. Zhang, Z. Liu, Y. Li, C. Li, R. Zou, J. Yu and Q. Xu, *Angew. Chem. Int. Ed.*, 2020, **59**, 7384-7389.
34. J. Li, H. Zhang, W. Samarakoon, W. Shan, D. A. Cullen, S. Karakalos, M. Chen, D. Gu, K. L. More, G. Wang, Z. Feng, Z. Wang and G. Wu, *Angew. Chem. Int. Ed.*, 2019, **58**, 18971-18980.
35. N. Zhang, T. Zhou, M. Chen, H. Feng, R. Yuan, C. a. Zhong, W. Yan, Y. Tian, X. Wu, W. Chu, C. Wu and Y. Xie, *Energy Environ. Sci.*, 2020, **13**, 111-118.
36. M. Qiao, Y. Wang, Q. Wang, G. Hu, X. Mamat, S. Zhang and S. Wang, *Angew. Chem. Int. Ed.*, 2020, **59**, 2688-2694.

37. N. Zhang, T. Zhou, J. Ge, Y. Lin, Z. Du, C. a. Zhong, W. Wang, Q. Jiao, R. Yuan, Y. Tian, W. Chu, C. Wu and Y. Xie, *Matter*, 2020, **3**, 509-521.
38. H.-W. Liang, S. Brüller, R. Dong, J. Zhang, X. Feng and K. Müllen, *Nat. Commun.*, 2015, **6**, 7992.
39. A. Zitolo, V. Goellner, V. Armel, M.-T. Sougrati, T. Mineva, L. Stievano, E. Fonda and F. Jaouen, *Nat. Mater.*, 2015, **14**, 937-942.
40. Y. J. Sa, D.-J. Seo, J. Woo, J. T. Lim, J. Y. Cheon, S. Y. Yang, J. M. Lee, D. Kang, T. J. Shin, H. S. Shin, H. Y. Jeong, C. S. Kim, M. G. Kim, T.-Y. Kim and S. H. Joo, *J. Am. Chem. Soc.*, 2016, **138**, 15046-15056.
41. Y. Zhou, X. Tao, G. Chen, R. Lu, D. Wang, M.-X. Chen, E. Jin, J. Yang, H.-W. Liang, Y. Zhao, X. Feng, A. Narita and K. Müllen, *Nat. Commun.*, 2020, **11**, 5892.
42. F. Luo, A. Roy, L. Silvioli, D. A. Cullen, A. Zitolo, M. T. Sougrati, I. C. Oguz, T. Mineva, D. Teschner, S. Wagner, J. Wen, F. Dionigi, U. I. Kramm, J. Rossmeisl, F. Jaouen and P. Strasser, *Nat. Mater.*, 2020, **19**, 1215-1223.
43. Y. H. Jeong, S. C. Kim and S. R. E. Yang, *Phys. Rev. B*, 2015, **91**, 205441.
44. Y. Li, X. Jiang, Z. Liu and Z. Liu, *Nano Res.*, 2010, **3**, 545-556.
45. C. Si, Z. Sun and F. Liu, *Nanoscale*, 2016, **8**, 3207-3217.
46. G. Wu, K. L. More, C. M. Johnston and P. Zelenay, *Science*, 2011, **332**, 443-447.
47. H. Zhang, H. T. Chung, D. A. Cullen, S. Wagner, U. I. Kramm, K. L. More, P. Zelenay and G. Wu, *Energy Environ. Sci.*, 2019, **12**, 2548-2558.
48. S. Liu, M. Wang, X. Yang, Q. Shi, Z. Qiao, M. Lucero, Q. Ma, K. L. More, D. A. Cullen, Z. Feng and G. Wu, *Angew. Chem. Int. Ed.*, 2020, **59**, 21698-21705.
49. J. Tian, A. Morozan, M. T. Sougrati, M. Lefèvre, R. Chenitz, J.-P. Dodelet, D. Jones and F. Jaouen, *Angew. Chem. Int. Ed.*, 2013, **52**, 6867-6870.
50. D. Xia, X. Yang, L. Xie, Y. Wei, W. Jiang, M. Dou, X. Li, J. Li, L. Gan and F. Kang, *Adv. Funct. Mater.*, 2019, **29**, 1906174.
51. K. Strickland, E. Miner, Q. Jia, U. Tylus, N. Ramaswamy, W. Liang, M.-T. Sougrati, F. Jaouen and S. Mukerjee, *Nat. Commun.*, 2015, **6**, 7343.